

RESEARCH ARTICLE

10.1002/2016JB013687

Key Points:

- Distinct element modeling of fault gouge consisting of velocity weakening (quartz analog) and velocity strengthening (talc analog) minerals
- Faults are weakened by ~20% of talc analog in uniform gouge mixtures or trace amount of talc in textured gouge mixtures
- Slip stability is transformed with ~20% of talc analog in uniform gouge mixtures or trace amount of talc in textured gouge mixtures

Correspondence to:

C. Wang,
cuw179@psu.edu

Citation:

Wang, C., D. Elsworth, and Y. Fang (2017), Influence of weakening minerals on ensemble strength and slip stability of faults, *J. Geophys. Res. Solid Earth*, 122, 7090–7110, doi:10.1002/2016JB013687.

Received 27 OCT 2016

Accepted 24 AUG 2017

Accepted article online 29 AUG 2017

Published online 13 SEP 2017

Corrected 18 SEP 2017

This article was corrected on 18 SEP 2017. See the end of the full text for details.

©2017. American Geophysical Union.
All Rights Reserved.

Influence of weakening minerals on ensemble strength and slip stability of faults

Chaoyi Wang¹ , Derek Elsworth^{1,2} , and Yi Fang¹ 

¹Department of Energy and Mineral Engineering, EMS Energy Institute, and G3 Center, Pennsylvania State University, University Park, Pennsylvania, USA, ²Department of Geosciences, Pennsylvania State University, University Park, Pennsylvania, USA

Abstract We explore the impact of phyllosilicate (weak but velocity strengthening) in a majority tectosilicate (strong but velocity weakening) matrix on bulk shear strength and slip stability of faults. Numerical simple shear experiments using a distinct element model (DEM) are conducted on both uniform mixtures of quartz and talc analogs and on textured mixtures consisting of a talc layer embedded in a quartz matrix. The mechanical response of particles is represented by a linear elastic contact model with a slip-weakening constitutive relation representing the essence of rate-state friction. The weight percentage of the talc in the uniform mixtures and the relative thickness of the talc layer in the textured mixtures are varied to investigate the transitional behavior of shear strength and slip stability. Specifically, for uniform mixtures, ~50% reduction on bulk shear strength is observed with 25% talc present, and a dominant influence of talc occurs at 50%; for textured mixtures, a noticeable weakening effect is shown at a relative layer thickness of 1 particle, ~50% shear strength reduction is observed with 3-particles, and a dominant influence occurs at 5 particles. In terms of slip stability, a transition from velocity weakening to velocity strengthening is observed with 10% to 25% talc present in the uniform mixtures or with 3 particles to 5 particles in the textured mixtures. In addition, further analysis suggests that quartz has a high tendency toward dilation, potentially promoting permeability; while talc dilates with increased slip rate but compacts rapidly when slip rate is reduced, potentially destroying permeability. The simulation results match well with previous laboratory observations.

1. Introduction

In nature, tectonic faults tend to slip at much lower resolved shear stress than the stresses inferred from rock mechanics experiments [Engelder *et al.*, 1975; Dieterich, 1979a; Marone *et al.*, 1990]. Explanations for this difference between laboratory observations and natural phenomena include the prevalence of low effective stresses, elevated pore pressures [Rice, 1992; Faulkner and Rutter, 2001], and dynamic weakening in which friction decreases above a threshold slip rate [Melosh, 1996; Di Toro *et al.*, 2006; Ampuero and Ben-zion, 2008]. Recent field observations of the San Andreas Fault [Moore and Rymer, 2007] and an exhumed low-angle normal fault in Italy [Collettini *et al.*, 2009] showed that the weakness of natural faults can be explained by the presence of talc, a frictionally weak mineral. Earlier experiments using synthetic mixtures of salts and muscovite/kaolinite [Bos and Spiers, 2002; Niemeijer and Spiers, 2006] showed that weakening in shear strength can occur with as little as 10% of frictionally weak minerals. In addition, the shear strength and associated stability of a fault greatly depends on its mineralogical composition [Ikari *et al.*, 2011]. Phyllosilicates like talc generally show low frictional strength but are stable during slip events—to the contrary, tectosilicates usually exhibit high frictional strength but slip unstably. Shear experiments using mixtures of talc and quartz sand [Carpenter *et al.*, 2009] suggest that in order to adequately weaken the fault, 30%–50% of frictionally weak minerals are needed. However, there is only ~2–3% of talc present in some weak tectosilicate faults suggesting that both the structure and texture of the talc is important.

This strong weakening effect of a frictionally weak mineral in a matrix where the majority of minerals are frictionally strong elicits the question of how much of the frictionally weak mineral is needed and in what structure? Also, importantly, what is the impact of this proportion and structure on the stability regime? Experiments conducted on synthetic gouge consisting of quartz as a frictionally strong phase and a through-going talc layer as a frictionally weak phase [Niemeijer *et al.*, 2010; Moore and Lockner, 2011] suggest that the frictional strength of the sample gouge decreases systematically with an increase in thickness of the

talca layer. Two critical values are noted for both the onset of weakening and for full weakening of the sample relative to pure talc. In addition to the decrease in frictional strength, the sample gouge also showed a transition from mildly unstable to mostly stable during slip events. Additional observations suggest that the permeability evolution of fractures is likely linked to such mineralogical effects on frictional stability [Fang *et al.*, 2017]. The slip characteristics of mature faults are governed by gouge, comprising granular and clay-sized particles, separating fault planes. Distinct element methods (DEM) [Cundall and Strack, 1979] have been successfully applied to represent the mechanical response of assemblages of circular-shaped particles that are characteristic of fault gouges. Numerical models of direct shear experiments on granular materials have been developed using DEM [Morgan and Boettcher, 1999] to investigate the effect of particle size distribution and the effect of interparticle friction coefficient on the deformation mechanisms in granular fault zones.

The full seismic cycle during fault slip is well described by rate-state friction laws [Dieterich, 1979b; Ruina, 1983; Scholz, 1998]. Rate-state friction laws have been incorporated into grain-grain contact models in DEM [Abe *et al.*, 2002; Morgan, 2004] and show good agreement with experimental observations with the configuration of flat fault surface. However, with synthetic fault gouges, the frictional response is shown to be highly dependent on the gouge structure and on particle rotation [Morgan, 1999, 2004]. Also, the full implementation of rate-state constitutive laws at a grain-grain scale is computationally inefficient. Despite available DEM models in simulating shear strength evolution of fault gouge, few DEM models are developed to simulate the strength and stability evolution of fault gouge consisting of two mineral phases, i.e., a frictionally strong phase and a frictionally weak phase. Our model simulates the shear strength and slip stability evolution of fault gouge consisting of uniform and textured mixtures of a frictionally strong phase and a frictionally weak phase. We especially focus on how much frictionally weak mineral is needed to weaken the fault. The results of this study provide a numerical approach which could be potentially beneficial for predicting the transitional behavior in stability and transport properties (especially permeability) of mineral mixtures with drastically different material properties during dynamic shearing. This study implements a DEM model with a slip-weakening law at the grain-grain boundary. In addition, sample layer thickness, porosity, and coordination number are monitored during numerical simulations. These simulations are used to define the transitional behavior in slip stability and poromechanical evolution of transport properties of the gouge.

2. Numerical Method and Materials

The distinct element method iteratively solves Newton's second law of motion for an assembly of particles with a predefined constitutive model applied at the grain-grain contacts. Calibration of the contact model is essential in DEM modeling. A model is established to simulate direct shear experiments on synthetic fault gouge comprising a two-phase mixture distributed both uniformly and as a through-going layer.

2.1. Distinct Element Method and Contact Model

The current DEM model has been developed using the Particle Flow Code 2-D (Itasca Corp.), with the principles of DEM described previously in a large body of literature [Antonellini and Pollard, 1995; Burbidge and Braun, 2002; Morgan and McGovern, 2005; Abe *et al.*, 2011]. DEM models are capable of simulating the mechanical response of granular materials, for example, fault gouge [Morgan and Boettcher, 1999; Guo and Morgan, 2004; Abe and Mair, 2009; Rathbun *et al.*, 2013; Sun *et al.*, 2016]. Such simulations are usually carried out using a two-dimensional (2-D) configuration with circular-shaped disks as particles. This maximizes computational efficiency but neglects the role of angularity and out-of-plane rotations in representing the real physical response of granular materials. In general, compared to a three-dimensional model, a two-dimensional representation is an adequate simplification which retains the advantage of significantly less computational cost while still obtaining a representative mechanical response.

A linear elastic contact model is implemented as the grain-grain contact model (Figure 1). Linear components act in normal and shear directions and reproduce linear elastic (no tension) and frictional behavior. All components act on a vanishingly small area, with only force transmitted. The contact force (F_c) is resolved into normal (F_n) and shear (F_s) components:

$$F_c = F_n + F_s \quad (1)$$

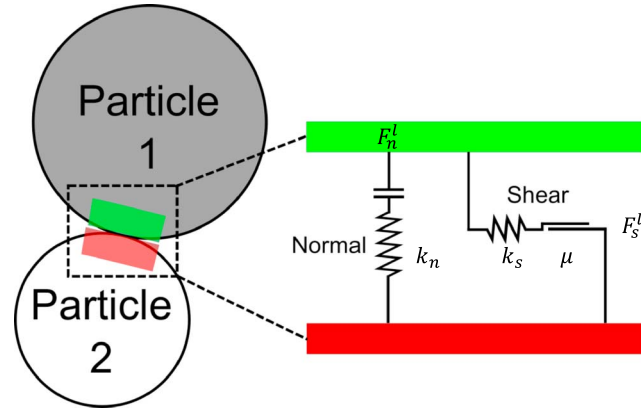


Figure 1. The components of linear elastic contact model.

The linear and shear components are updated in the absence of slip and with active contact as

$$F_n = (F_n)_0 + k_n \Delta \delta_n \quad (2)$$

$$F_s = (F_s)_0 + k_s \Delta \delta_s \quad (3)$$

$$F_s^\mu = -\mu F_n \quad (4)$$

where k_n and k_s are the stiffness of normal and shear elastic components and $\Delta \delta_n$ and $\Delta \delta_s$ are the relative normal and shear displacement between the contacting grains within one time step.

The calculated shear force is compared to the shear strength of the current contact state (F_s^μ) and determines whether slip is initiated.

If slip occurs, unlike Coulomb friction with a constant coefficient of friction (μ), a rate-state friction law [Dieterich, 1978; Ruina, 1983] is utilized to describe the evolution of friction coefficient during the slip event. The original rate-state constitutive relation is described by the empirical state variable-based friction evolution (equation (5)) with elastic coupling (equation (6)):

$$\mu = \mu_0 + a \ln\left(\frac{V}{V_0}\right) + b \ln\left(\frac{V_0 \theta}{D_c}\right) \quad (5)$$

$$\frac{d\mu}{dt} = k(V_{lp} - V) \quad (6)$$

where a and b are the empirical stability parameters of the material, usually determined by experiments and depend on mineralogy; D_c is the critical slip distance which indicates how much distance the contacting surface slips until reaching the next steady state. The second term on the right-hand side in equation (5) describes the evolution of friction coefficient upon a stepped velocity change (the direct effect), and the third term describes the evolution of friction coefficient over the critical slip distance D_c (evolution effect). V , V_0 , and V_{lp} are the relative current, reference, and load point velocities of the two contact surfaces, respectively; θ is the state variable; k is the geometric stiffness of the loading system. When k is smaller than a critical value, unstable sliding will occur if the system is velocity weakening; the critical stiffness is governed by confining stress, critical slip distance, and stability parameters a and b . There are two evolution laws for the state variable, Dieterich law and Ruina law, which are shown as equations (7) and (8) below, respectively:

$$\frac{d\theta}{dt} = 1 - \frac{V\theta}{D_c} \quad (7)$$

$$\frac{d\theta}{dt} = -\frac{V\theta}{D_c} \ln\left(\frac{V\theta}{D_c}\right) \quad (8)$$

Experimental observations show that rate-state friction adequately describes both seismic behavior and friction healing of fault slip events [Marone, 1998a]. However, the complexity of solving the full nonlinear constitutive relations makes the full implementation in DEM at the grain-grain scale computationally expensive [Abe et al., 2002]. To reduce this computational cost, and assuming the stiffness of the system is much larger than the critical stiffness, the rate-state evolution may be simplified as a form of slip-weakening law

$$\mu_p = \mu_{ref} + a \ln\left(\frac{V_{lp}}{V_{ref}}\right) \quad (9)$$

$$\mu_{ss} = \mu_{ref} + (a - b) \ln\left(\frac{V_{lp}}{V_{ref}}\right) \quad (10)$$

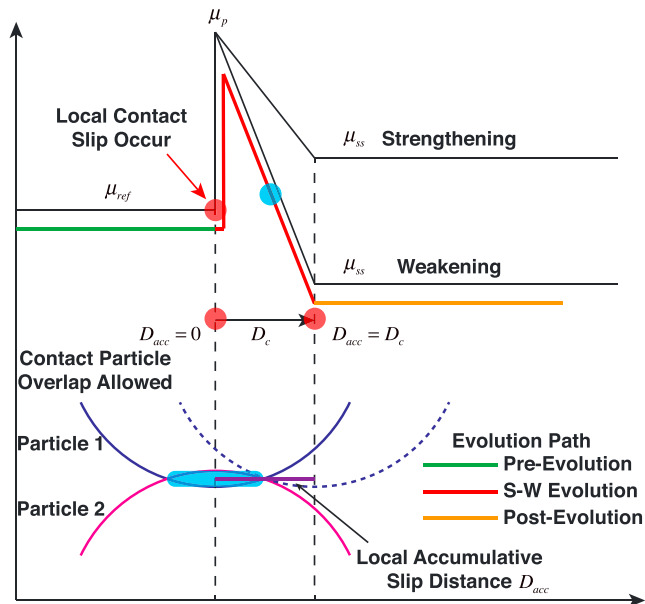


Figure 2. Schematic of the slip-weakening law: the friction coefficient of a local contact that starts to evolve upon a slip event together with a difference between global load point velocity and stored global reference velocity, friction will reach a peak value (μ_p) and continue to evolve to its steady state (μ_{ss}) if local slip persists according to either velocity strengthening or velocity weakening; if slip halted before reaching steady state, the friction coefficient will stay as is; friction evolution of newly formed contact will be reset and started from the beginning (left to right) if reinitiated.

$$\mu = \begin{cases} \mu_p & D_{acc} = 0 \\ \mu_p - \left(\frac{\mu_p - \mu_{ss}}{D_c}\right) D_{acc} & D_{acc} \in (0, D_c) \\ \mu_{ss} & D_{acc} = D_c \end{cases} \quad (11)$$

where μ_p is the peak friction due to the direct effect of velocity change, μ_{ss} is the steady state friction after frictional evolution has completed, μ_{ref} is the reference friction coefficient depending on different mineral analogs, and D_{acc} is the relative local shear displacement that has accumulated since that previous velocity change on each contact. This value varies through every contact in the model depending on local contact state. V_{ip} and V_{ref} are the absolute values of the current and previous shear velocity of the shear platens, respectively. D_c is the characteristic slip distance—a mineral-related property that is assigned to each and every local contact.

Figure 2 shows the implementation of this slip-weakening model. The contact model is implemented onto each contact of the assembly. V_{ip} and V_{ref} are stored for each contact; thus, each contact “knows” the current global shear velocity as well as the velocity history of the previous velocity step. D_{acc} is the accumulated relative local shear displacement. D_{acc} remains zero if no local slip has occurred (shown in Figure 2 as the green path)—as a result, the friction coefficient will remain at a value of μ_{ref} . If (i) a slip event occurs at a contact, and (ii) there is a difference between stored V_{ip} and V_{ref} , the contact will slip weaken (following the red path in Figure 2, as described by equations (9) to (11)). If the local slip distance threshold D_c is reached, the contact friction will remain as μ_{ss} (orange path) as long as the contact is still active. If slip terminates in the middle of the evolution path (but the contact is still active), then the friction coefficient on the contact will remain as is (illustrated by the blue dot on the red path in Figure 2) until slip reinitiates. At reinitiation, the contact friction continues to follow the red evolutionary path. There are cases when active contacts undergoing slip-weakening evolution turn inactive due to particle rearrangement. In these cases, the slip-weakening evolution will cease once the contact becomes inactive. Newly formed contacts will begin evolving from the end of the green path (Figure 2) once conditions (i) and (ii) above are both met for the contact. Otherwise, the friction coefficient will remain constant as μ_{ref} . If a contact transits a full evolution path (D_c), the friction coefficient will remain as μ_{ss} no matter the slip state and as long as the contact is still active. The contact

Table 1. Model Parameters Including Calibrated Elastic Modulus for Quartz [Hieher, 1996] and Talc [Guan et al., 2012]

	Quartz Analog	Talc Analog	Unit ^a
Density	2650	2800	kg/m ³
Radius	50–100	20–25	μm
Interparticle friction	0.3	0.05	NA
Effective modulus	1.30E + 10	1.00E + 09	N/m ²
Normal-to-shear stiffness ratio	1	1.5	NA
Calibrated elastic modulus	8.35	0.79	GPa
Interparticle <i>a</i> value	0.025	0.025	NA
Interparticle <i>b</i> value	0.050	0.005	NA
Interparticle <i>D_c</i>	50	25	μm

^aNA, not applicable.

will not evolve again until the next global velocity step. In particular, once a new contact is formed, the accumulated relative local shear displacement (D_{acc}) is reset to zero so that the slip history of the contact, either slipping or nonslipping, is reinitialized to enable renewed evolution.

2.2. Mineral Analogs

Observations in nature suggest that the presence of talc may greatly reduce the shear strength of mostly tectosilicate faults and may be a cause of fault creep [Moore and Rymer, 2007]. Measurements of the shear strength and stability of granular quartz reveal that quartz is a typical tectosilicate which exhibits high frictional strength and velocity-weakening properties. Conversely, talc is usually frictionally weak but velocity strengthening [Ikari et al., 2011; Moore and Lockner, 2011]. Because quartz and talc have these key contrasting frictional and stability properties, they represent the most suitable candidate analogs for this study. The density, particle size, and rate-state parameters used in this study for quartz and talc analogs are listed in Table 1.

The elastic modulus of granular materials is dependent on mean stress and is usually much smaller than that of the intact crystals [Hieher, 1996; Guan et al., 2012]. In DEM modeling, the elastic behavior of the granular assembly is represented by effective modulus and normal-to-shear stiffness ratio. The effective modulus and normal-to-shear stiffness ratio are assigned at each contact, and the relationship between them and contact stiffness is listed below (equations (12) and (13)) as

$$k_n = \frac{AE^*}{L} \tag{12}$$

$$k_s = \frac{k_n}{\kappa^*} \tag{13}$$

where k_n is the normal contact stiffness, k_s is the shear stiffness, A is the virtual contact area of the two entities, typically the product of the smaller diameter of the two contacting entities and unit thickness, and κ^* is the normal-to-shear stiffness ratio.

Notably, the effective modulus is not a macroscopic elastic modulus but is related to it, and the normal-to-shear stiffness ratio is related to Poisson's ratio. Specifically, the normal-to-shear stiffness ratio is defined as the ratio of the normal stiffness (k_n) and shear stiffness (k_s) of the elastic components shown in Figure 1. These are contact parameters that are assigned directly to the contacts. They are derived by performing numerical biaxial compression experiments on packs of quartz and talc analogs, respectively. In the trial-and-error calibration procedure, initial estimates of effective modulus and normal-to-shear stiffness ratio are made as trial parameters. Then a face-centered cubic assembly of pure mineral analog is generated with the trial parameters. The loose assembly is compacted, equilibrated, then a biaxial compression test is conducted under a normal stress of 10 MPa. The macroscopic elastic modulus of the cubic sample is then calculated by the slope of the axial stress-strain evolution curve (loading direction) at 0.05% of the axial strain. This macroscopic elastic modulus is then compared with laboratory-measured macroscopic elastic modulus in the literature. We generally accept values of calibrated modulus which lie within 3% of the suggested values of laboratory experiments [Hieher, 1996; Guan et al., 2012]; otherwise, we adjust the initial estimates

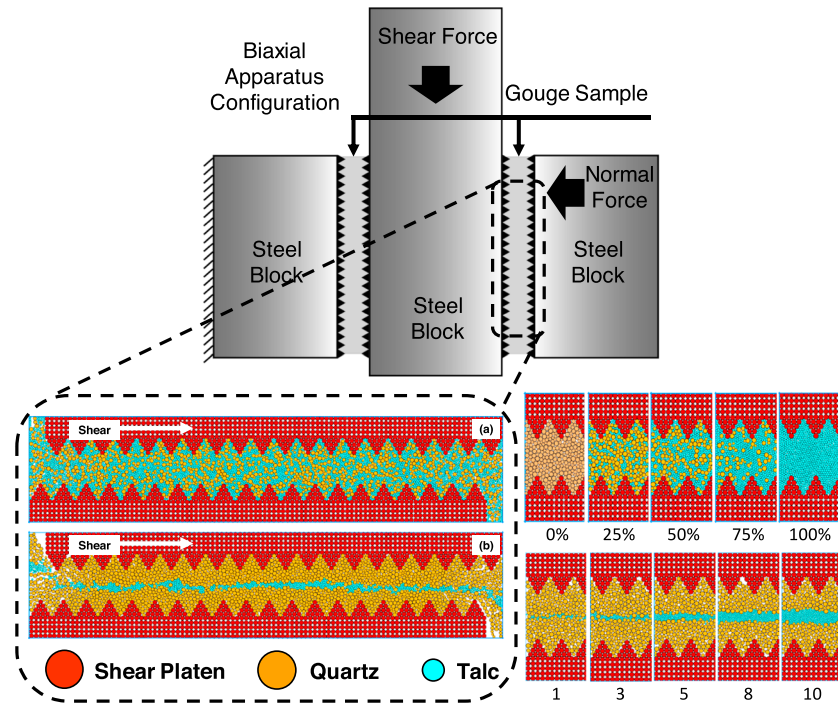


Figure 3. DEM model configuration as a symmetric simplification of a double direct shear apparatus: (a) uniform mixtures, (b) textured (layered) mixtures. Inset on the right-hand side shows the variation of quartz (orange) to talc (blue) content/relative layer thickness in uniform/layered mixtures.

and repeat the calibration process. The estimates of effective modulus, normal-to-shear ratio, and resultant modulus used in this study are shown in Table 1. In addition, the effective modulus of the wall element-particle contact is set to the same magnitude as the quartz-quartz contact analog to minimize stress concentrations effects.

In the case where a talc and quartz analog particle is in contact, the stiffness and rate-and-state parameters (a and b) of this contact are expressed by the geometric average from both contacting entities. The friction coefficient (μ) and characteristic slip distance (D_c) are determined by the smaller value of either entity.

3. Experiment Design

The model configuration is in double direct shear configuration [Mair and Marone, 1999], which consists of a pair of sawtooth-shaped platens and a synthetic fault gouge sample sandwiched between them (Figure 3). Unlike the full experimental setup, the numerical model represents one symmetric limb of the apparatus with the modeled platens retained parallel. Before the shear experiment, the model is 20 mm in length (horizontal) and approximately 5 mm in height (vertical). The shear platens in the numerical model consist of arrays of tightly bounded particle clusters (clumps) with a triangular tip. Wall elements are specified outside the platens to serve as boundaries. These wall elements are facets which do not obey Newton's second law of motion due to lack of mass; however, a servo mechanism constantly adjusts the velocity of the wall elements to maintain static normal stress. Specifically, total unbalanced normal force on a specific wall is monitored by superposing contact normal forces of contacting particles. The velocity vector of the wall element is then adjusted by a scaled value of the difference between total unbalanced stress and target normal stress. A constant confining/normal stress of 10 MPa is applied in all numerical runs. The velocities of the top and bottom wall boundaries are adjusted simultaneously and consistently during shear experiments in order to maintain the normal stress during the shear experiment. A typical numerical shear experiment is conducted as follows:

1. It generates shear platens and adjacent wall elements.
2. It generates loosely distributed analog particles between two shear platens.

Table 2. Model Parameters of Numerical Experiments; Quartz/Talc Content is Varied From 0% to 100% in Uniform Mixtures; Relative Talc Layer Thickness is Varied From 1 particle to 10 particles in Layered Mixtures; Initial Sample Thickness and Shear Velocity Regime During the Tests are Listed

Name	Quartz Analog (wt %)	Talc Analog (wt %)	Relative Talc Layer Thickness ^a	Sample Thickness ^b (μm)	Shear Velocity (μm/s)
cqt100-00	100%	0%	NA	5283.78	1
cqt90-10	90%	10%	NA	5205.57	1
cqt80-20	80%	20%	NA	5163.03	1
cqt75-25	75%	25%	NA	5133.04	1
cqt60-40	60%	40%	NA	5117.93	1
cqt50-50	50%	50%	NA	5107.28	1
cqt25-75	25%	75%	NA	5123.29	1
cqt00-100	0%	100%	NA	5146.91	1
sqt100-00	100%	0%	NA	5175.16	1/10/1/10/1
sqt90-10	90%	10%	NA	5109.28	1/10/1/10/1
sqt80-20	80%	20%	NA	5051.87	1/10/1/10/1
sqt75-25	75%	25%	NA	5041.20	1/10/1/10/1
sqt50-50	50%	50%	NA	5006.85	1/10/1/10/1
sqt25-75	25%	75%	NA	5021.85	1/10/1/10/1
sqt00-100	0%	100%	NA	5045.55	1/10/1/10/1
cqt001	98%	2%	1	5168.64	1
cqt003	97%	3%	3	5163.03	1
cqt005	94%	4%	5	5139.05	1
cqt008	90%	10%	8	5152.66	1
cqt010	87%	13%	10	5144.23	1
sqt001	98%	2%	1	5168.64	1/10/1/10/1
sqt003	97%	3%	3	5163.03	1/10/1/10/1
sqt005	94%	4%	5	5139.05	1/10/1/10/1
sqt008	90%	10%	8	5152.66	1/10/1/10/1
sqt010	87%	13%	10	5144.23	1/10/1/10/1

^aThe relative thickness of talc analog layer is determined by the most approximate number of particles vertically aligned in the actual talc analog layer.

^bThe sample thickness is measured at the beginning of each numerical run. NA, not applicable.

- It applies controlled normal velocity (vertical) on wall elements to drive both shear platens to compact loose particles until reaching the desired confining stress. The velocity applied to wall elements is adjusted to maintain the desired confining stress until average ratio is sufficiently low (0.001). The average ratio is defined as the average of the ratio of unbalanced forces to the sum of body force, applied force, and contact forces on one particle in all degrees of freedom. This quantity is used to identify whether the system is close to equilibrium. The average ratio of 0.001 is typically used in this study to judge whether the system is sufficiently close to equilibrium.
- It actuates the upper shear plate with a prescribed velocity scheme while holding the lower platen static in order to exert internal shear of the gouge particles.
- It records experimental parameters until shear displacement reaches the desired shear displacement or completion of desired velocity steps.

Laboratory experiments reveal that the distribution of talc in the fault slip zone plays an important role in determining the shear strength and slip stability [Moore and Rymer, 2007]. Reduction in shear strength but enhancement in slip stability results from an increase in talc content, especially when talc forms a layered structure in a tectosilicate matrix. This effect of both uniformly distributed and layered talc on the shear strength and slip stability of the fault are the foci of this study. Uniform and layered mixtures of talc and quartz analogs are tested with systematically increased talc content (weight percentage) and relative layer thickness (Figures 3a and 3b, right-hand side insets). Constant velocity shear experiments (1 μm/s for 1500 s) and velocity-stepping (1/10/1/10/1 μm/s for 1600 s) experiments were performed on both uniform and layered mixtures. The bulk friction coefficient is calculated from the ratio of monitored shear stress and normal stress. The numerical simulations and their associated parameters are listed in Table 2. Additionally, prior results [Guo and Morgan, 2004] suggest that 2-D geometry and circular particles in DEM engender a high tendency to rolling, reducing bulk friction coefficient. In this model, the rotation of all mineral analogs is restricted in order to eliminate the rolling tendency of circular particles.

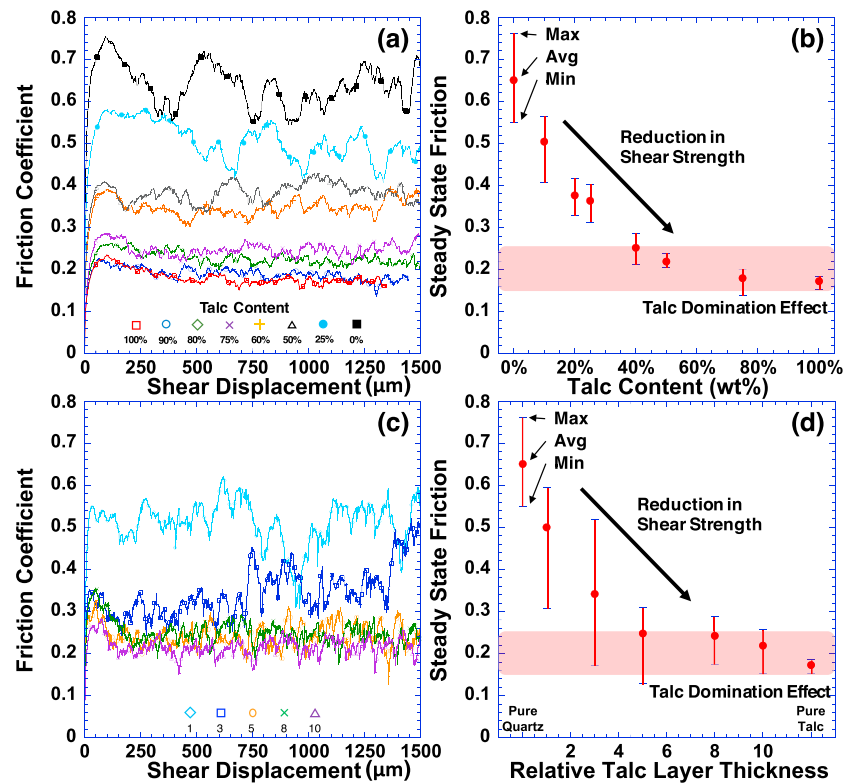


Figure 4. (a) Friction evolution of uniform mixtures (note: symbols in the figure represent keys). (b) Residual friction decreases as the talc content increases, with a noticeable weakening at ~25% and a dominant weakening at ~40%. (c) Friction evolution of textured mixtures. (d) Residual friction decreases as the thickness of the talc layer increases, with a noticeable weakening at 3 particles and a dominant weakening at 5 particles. (note: the maximum, average and minimum values shown in the error bar are calculated from each friction evolution data set after shear displacement of 750 μm).

4. Results

Numerical simulations of biaxial direct shear experiments are conducted for mineral mixtures of quartz and talc. Two mixture patterns are considered—uniform and layered. Shear strength evolution and the transition of stability parameters are shown in the results with a variation of mineral compositions and mixture patterns.

4.1. Frictional Evolution of Mineral Mixtures

Constant velocity shear experiments are conducted on uniform mixtures with a shear velocity of 1 $\mu\text{m/s}$. The evolution of shear strength of uniform mixtures is shown in Figure 4a. It is apparent that the bulk shear strength (friction coefficient) decreases as the weight percentage of talc in the mixture increases. To be specific, the residual friction coefficient remains at ~0.70 with no talc in the mixture, while it reduces from ~0.70 to ~0.35 with ~25% talc, showing a strong weakening effect of talc on bulk shear strength of the sample. However, the fast reduction in shear strength slows down when there is more than 25% talc present in the mixture (e.g., 30% and 40%); when the weight percentage of talc analog exceeds 75%, the residual friction coefficient of friction exhibits a similar magnitude to pure talc, showing a talc-dominating effect. This transition in steady state friction is plotted in Figure 4b. This trend is revealed in previous experimental observations [Carpenter *et al.*, 2009; Moore and Lockner, 2011].

Similarly, constant velocity shear experiments with the same velocity scheme are conducted on textured (layered) mixtures. Specifically, the sample consists of a quartz matrix and a sandwiched layer of talc. The relative thickness of the talc analog layer is varied in each numerical run to investigate its effect on shear strength of the mixture. The evolution of friction is shown in Figure 4c. Figure 4d clearly shows that the steady state friction coefficient decreases as the relative thickness of the talc analog layer increases. In particular, the steady state friction coefficient drops from ~0.70 to ~0.35 with layer thickness of the talc increasing from

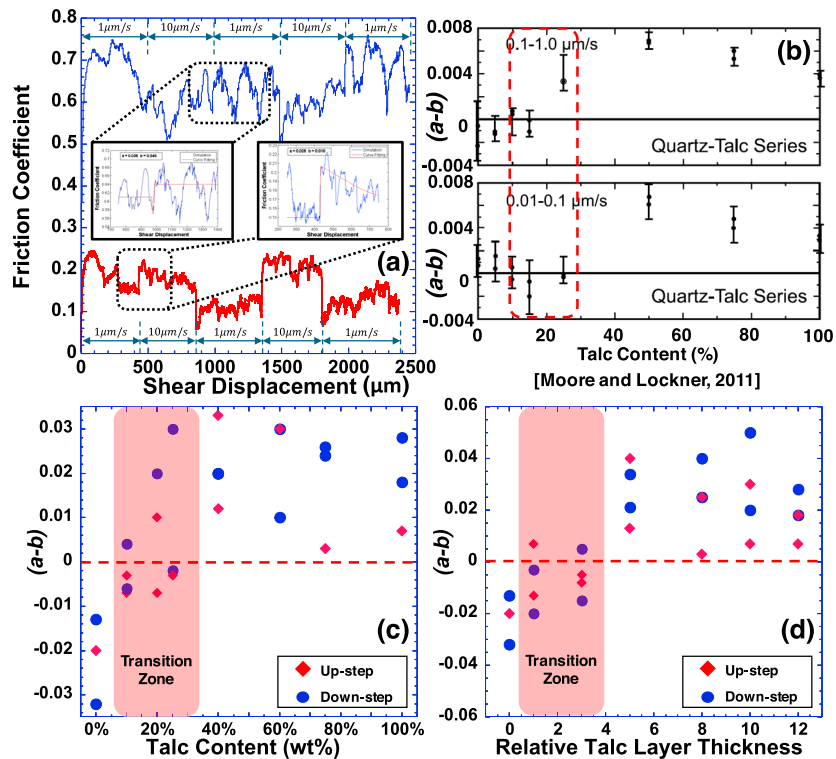


Figure 5. Slip stability evolution of uniform mixtures: (a) end-member friction evolution with velocity-stepping shear tests (inset shows examples of curve fitting to recover stability parameters). (b) Laboratory data [Moore and Lockner, 2011] of $(a - b)$ obtained using quartz and talc mixtures. The red dashed rectangular is the transition zone from velocity weakening to velocity strengthening. (c) Evolution of stability parameter $(a - b)$, $(a - b)$ values are negative with no talc present but shifts to positive after more than 10% of talc is introduced and will keep being positive when more than 25% talc is introduced. (d) Evolution of stability parameter $(a - b)$, $(a - b)$ values are negative with no talc present but shift to positive after introducing a thin layer (1 particle and 3 particles) of talc and will remain positive when relative talc layer thickness is larger than 5 particles.

0 particle to 3 particles. With a relative layer thickness of 5 particles, the residual friction coefficient is reduced to ~ 0.25 , which is approximately the steady state friction of pure talc (~ 0.20). With a relative layer thickness larger than 5 particles, the residual friction coefficient drops incrementally and approaches the steady state friction for pure talc. These observations suggest that a relative thickness of 5 particles is sufficient for the talc analog to establish a dominant effect. Similar effects are also observed with relative thicknesses of 8 particles and 10 particles. This trend is consistent with previous experimental observations [Niemeijer et al., 2010].

4.2. Slip Stability Evolution of Mineral Mixtures

Observations from the constant velocity numerical experiments suggest that talc has a significant weakening effect on the shear strength of a quartz-rich fault. In addition, it is suggested from experiments [Moore and Lockner, 2011] that talc also influences slip stability of faults consisting of a small amount of talc in a frictionally strong matrix, i.e., slip stability can transit from velocity weakening (quartz dominant) to velocity strengthening (talc dominant) with increasing talc content.

Virtual velocity stepping experiments, with shear velocity steps of $1 \mu\text{m/s}$ and $10 \mu\text{m/s}$, were performed on both uniform and layered mixtures of talc and quartz analogs. Specifically, weight percentage of talc in uniform mixtures and relative layer thickness of talc are varied to explore the transition from velocity weakening to velocity strengthening. Figure 5a shows the friction evolution of two end-member uniform mixtures of pure quartz and pure talc as an example. The $(a - b)$ values are analyzed by zooming into each of the velocity steps, and the velocity steps are fitted to rate-state friction constitutive relations. We fit the rate-and-state parameters using a forward Levenberg-Marquardt algorithm [Press et al., 1987]. We make an initial estimate of a , b , and D_c values and progressively fit to rate-and-state constitutive relations (5) to (8). The constitutive

relation is solved with shear displacement using a fourth-order Runge-Kutta algorithm [Press *et al.*, 1987]. The Levenberg-Marquardt algorithm searches in the range from 1/10 of the initial estimate to 10 times the initial estimate. We conclude when either the difference of parameter or the Chi-square value of the data from current estimate and last estimate meet the tolerances of 0.0001 or 0.01, respectively. The insets in Figure 5a show the stability analysis of two velocity steps, for example.

In terms of the transition of slip stability parameters, i.e., $(a - b)$ values, Figure 5b shows the $(a - b)$ values obtained by previous laboratory shear experiments on mixtures of quartz and talc [Moore and Lockner, 2011]. The transition is clearly observable at ~20% talc. In our simulation, the transition in stability parameter of uniform mixtures is shown in Figure 5c; the $(a - b)$ values are negative (velocity weakening) when no talc is introduced; however, the $(a - b)$ values transit to positive rapidly when there is ~10% to ~25% talc present in the mixture. With more than 25% talc analog introduced, the $(a - b)$ values of the bulk sample remain positive, indicating the dominating effect of talc (velocity strengthening) on bulk slip stability of the mixture.

Transition in slip stability is also expected in layered mixtures of quartz and talc. Results from velocity-stepping experiments on uniform mixtures show a similar trend of increasing $(a - b)$ values when increasing the relative talc layer thickness. With a through-going talc layer, the $(a - b)$ values of the gouge transit to positive with a trace amount of talc (1–3 particles, Figure 5d). The sample exhibits velocity strengthening similar to the pure talc with relative talc layer thickness of 5 particles. Additionally, the $(a - b)$ values become larger compared to those for uniform mixtures when the relative thickness of the talc layer is increased. This behavior indicates that the spatial distribution of talc in the gouge has significant influences on the slip stability of the mixture. With a layered structure, even a minimal amount of talc can alter the bulk stability behavior of the fault.

4.3. Dilation, Coordination Number, and Permeability

Slip events are usually accompanied by fault dilation or compaction depending on the mineralogical composition and corresponding mechanical properties. The distinctive difference between dilation and compaction defines a possible link between the mineralogy and the permeability evolution of the fault. In other words, dilation indicates potential increase in fault permeability and vice versa. Usually, dilation or compaction can be directly measured in laboratory experiments through monitoring the evolution of sample layer thickness. However, it is difficult to directly observe the evolution of porosity and average coordination number in laboratory experiments. Coordination number is the average number of contacts around a particle. The evolution of porosity and coordination number give a clearer picture of dilation or compaction at grain-grain scale. Specifically, when the bulk gouge is compacted, the coordination number is expected to increase while porosity decreases and conversely for dilation.

Figures 6a–6c show the evolution of sample layer thickness, average coordination number, and porosity evolution for pure quartz and pure talc during velocity-stepping experiments, respectively. Overall layer thickness decrease is observed during our numerical tests, which causes a reduction in shear zone thickness. This decrease in sample layer thickness over shear displacement is induced by mineral analog particles filling the two empty pockets at the ends of the upper and lower shear platens during dynamic shearing. This effect occurs in every numerical test; therefore, we consider it as a background compaction effect that will not significantly affect the comparison of dilation effects between numerical tests. Distinct differences are noted for end-member behaviors. Quartz and talc samples begin with similar initial layer thicknesses (Figure 6a); despite background compaction effects, quartz shows an increase in layer thickness and a sharp decrease in coordination number during the first ~500 μm in shear displacement. Conversely, talc samples show the opposite trend in layer thickness evolution. In addition, the evolution of the coordination number at a velocity up step, as highlighted for talc in Figure 6b, shows a slow decrease (i.e., from 1 $\mu\text{m/s}$ to 10 $\mu\text{m/s}$) but a sharp increase with a velocity down step (i.e., from 10 $\mu\text{m/s}$ to 1 $\mu\text{m/s}$). This indicates a slow decrease in number of contacts (dilation) during velocity up steps but a fast increase in the number of contacts (compaction) upon velocity down steps. The same behavior is not clearly observed for quartz or for other quartz-rich samples. This is further discussed in section 5.5.

Moreover, we can directly monitor the porosity in the assembly by calculating the ratio of void volume and total volume. An increase in porosity is observed Figure 6c for quartz samples throughout the loading, while relatively steady porosity evolution is observed for the talc sample. The quartz sample evolves to a higher

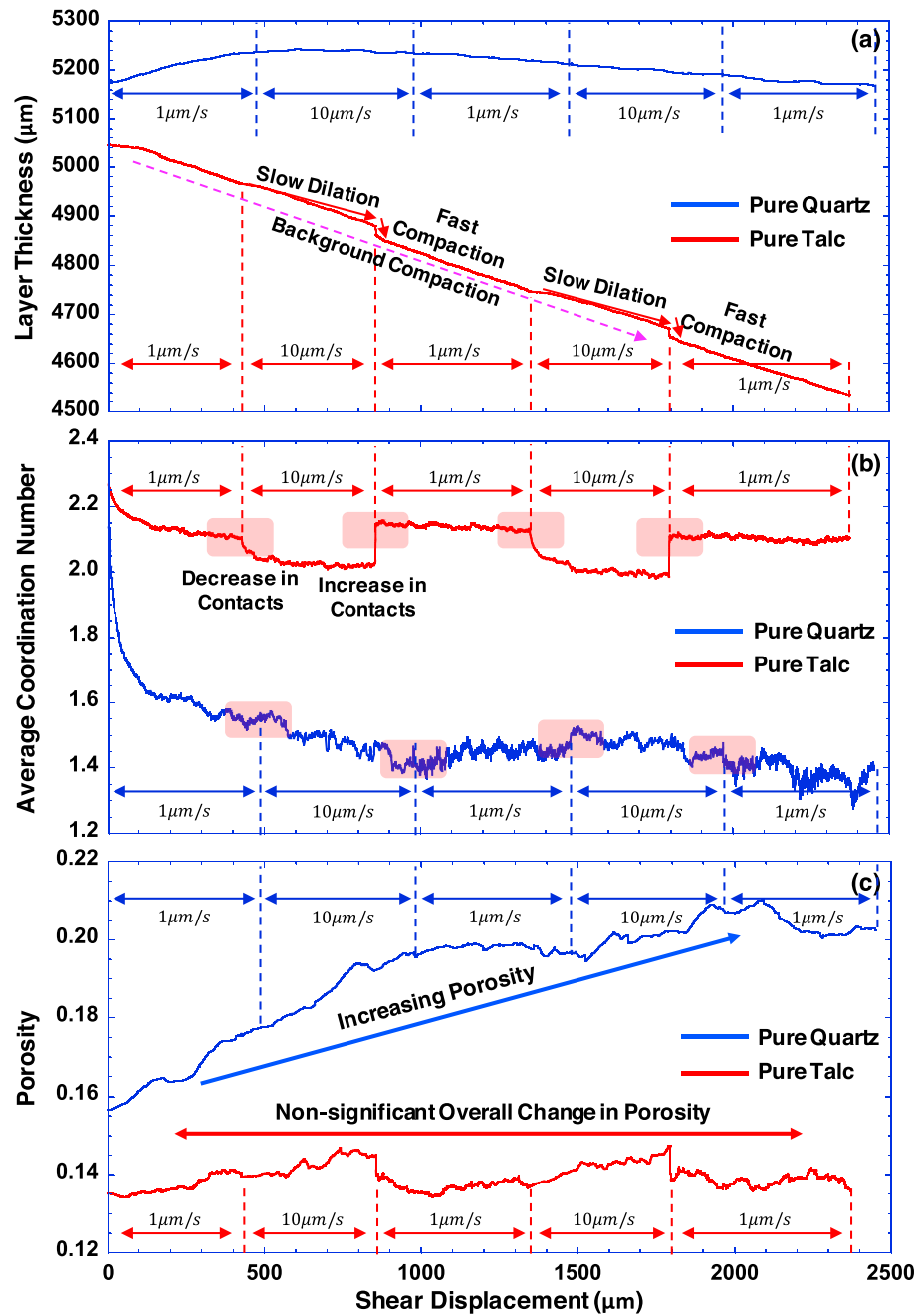


Figure 6. (a) Evolution in layer thickness of a pure quartz/talc sample during velocity stepping experiments; quartz shows strong dilation despite background compaction, while talc shows slow dilation upon velocity up steps and fast compaction upon velocity down steps. (b) Evolution of average coordination number of the same tests; talc shows a gradual decrease in coordination number at velocity up steps but a rapid increase in coordination number at velocity down steps; quartz shows a negligible change in coordination number at velocity steps. (c) Sample porosity evolution of the same tests, quartz shows overall increasing porosity while talc shows relatively insignificant porosity change throughout the test.

layer thickness, porosity, and lower coordination number than the talc sample, indicating a stronger dilation effect. Evolutions of these three parameters for uniform mixtures and textured mixtures lie between the two end-member evolution responses.

Estimates of permeability evolution are shown in Figure 7 using equations (14) and (15) [Ouyang and Elsworth, 1993; Samuelson et al., 2011]

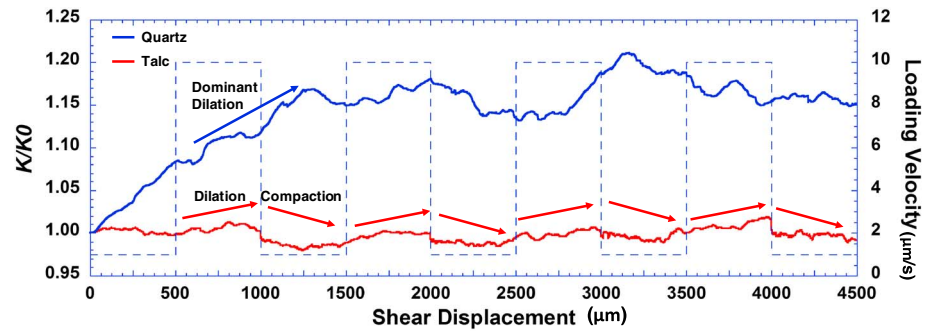


Figure 7. Permeability evolution of gouge consisting of pure quartz or talc: gouge consisting of quartz is dilation dominated, while gouge consisting of talc exhibits dilatation only on velocity up steps but rapid compaction on velocity down steps.

$$\frac{k}{k_0} \cong \left(1 + \frac{\Delta H}{H}\right)^3 \tag{14}$$

$$\frac{\Delta H}{H} \cong \Delta\phi \tag{15}$$

where k/k_0 is the relative ratio in permeability, $\Delta H/H$ is the relative ratio in sample thickness, and $\Delta\phi$ is the relative difference in porosity. Figure 7 shows that the permeability of pure quartz increases regardless of the change in velocity, while the permeability of the pure talc sample remains stable with a slight increase during velocity up steps and a sharp decrease during velocity down steps. While a compaction effect is generally expected during velocity down steps, the observations can be plausibly explained by the tight packing of the quartz sample in our specific runs; thus, only dilatation is observed. Furthermore, the strong tendency of the dilatation of quartz can also be explained by a higher elastic modulus and higher particle interlocking caused by higher friction resistance at contacts.

4.4. Effect of Normal Stress, Characteristic Slip Distance, and Particle Size

We test the model with variations in normal stress, critical slip distance, and particle size to analyze the sensitivity of the DEM model. We examine behavior at normal stresses of 5, 10, 15, 30, and 50 MPa. The frictional evolution curves for 75% quartz and 25% talc mixtures under these different normal stresses are shown in Figure 8a. From the initial frictional evolution, we observe a trend indicating that it takes less shear displacement for the assembly to reach steady state friction at lower normal stress—this may be attributed to less normal constraints on particles to rearrange under shearing. The remainder of the evolution curve shows bulk shear strengths to be generally higher during velocity up steps at low normal stress (5 MPa)—this is likely due to the stronger tendency for dilatation at low normal stresses. Despite these observations, the friction evolution curves generally overlaid each other and feature no general trend in shear strength and stability parameters.

In terms of characteristic slip distance (D_c), Figure 8b shows the frictional evolution curves for 75% quartz and 25% talc mixture under a normal stress of 10 MPa with 2 times, 1 times, and 0.5 times the values of D_c (refer to Table 1). Again, the frictional evolution curves overlaid each other. We observe no significant difference in the frictional evolution due to the change in D_c . This is possibly caused by the contact mechanism described in section 5.5. In the case of smaller D_c , the assembly requires a shorter slip distance to reach steady state, which is subtly observed from the first and the second velocity down steps. However, the significant amplitude of noise masks this.

The effect of particle size on the evolution of friction is shown in Figure 8c, for 2 times, 1 times, and 0.5 times particle radius (refer to Table 1) under a normal stress of 10 MPa. For smaller particle sizes, the amplitude of the fluctuation is reduced. The evolution curve is not generally offset by reducing the particle diameter except in the initial velocity step, where for 0.5 times particle radius the friction coefficient is smallest. This is potentially due to the increase in surface area of the talc particles when the number of particles increases. However, this initial offset is soon annulled.

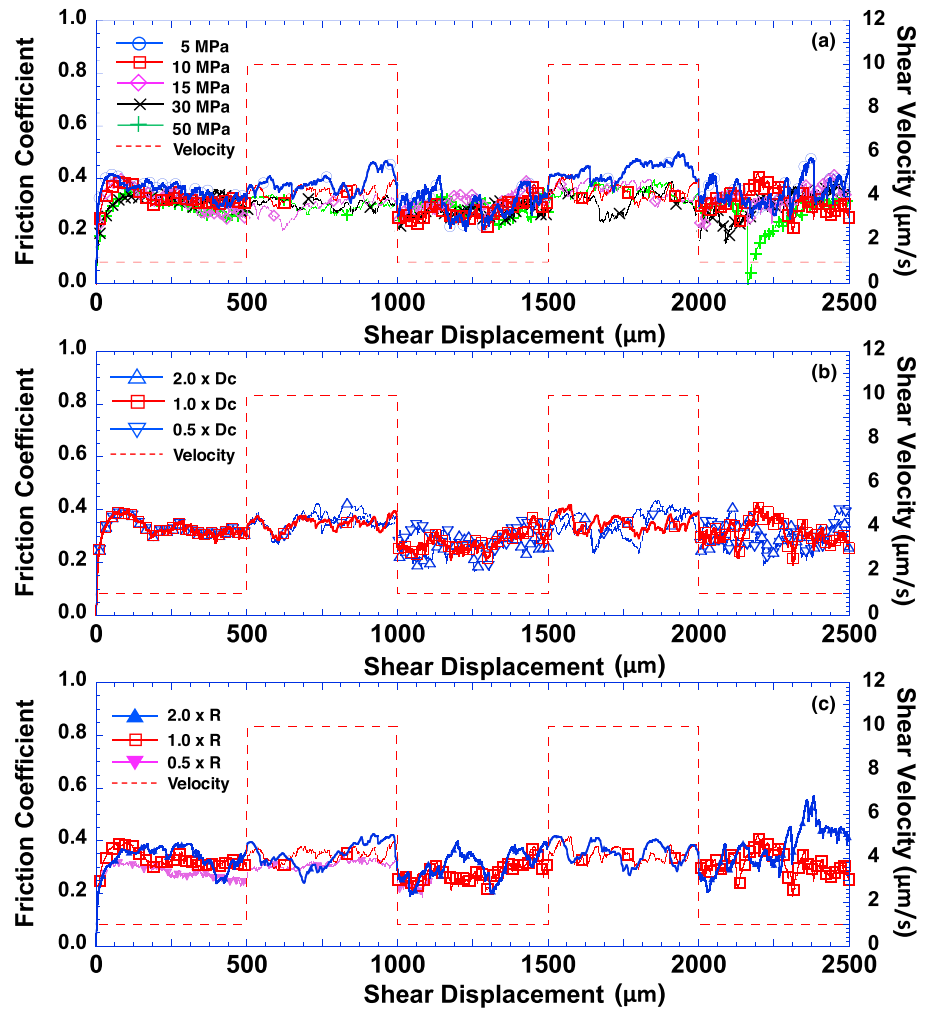


Figure 8. Friction evolution of a uniform mixture containing 75% quartz and 25% talc, at (a) normal stresses of 5, 10, 15, 30, and 50 MPa; (b) with D_c set at 0.5, 1.0, and 2.0 times characteristic slip distance; and (c) with particle sizes of 0.5, 1.0, and 2.0 times particle size.

5. Discussion

The numerical simulation results suggest that evolution of shear strength and stability of the simulated fault gouge is largely related to weight percentage and texture of the talc in the mixture. It is observed that for uniform mixtures, a relatively small amount of talc (~25% in weight percentage) can significantly weaken the fault; while for layered mixtures, a minimal amount of talc (a relative thickness of 3 particles) can provide the same level of influence. These results in turn pose questions of what are the possible mechanics behind the observed evolution trends and their implications. The following discussion examines the slip-weakening law, by examining fluctuations within the numerical friction measurements, the influence of localization effects of shear due to heterogeneity, the effect of platen rigidity and system stiffness, the stability of the calculated slip and mechanism for frictional healing, and the scaling of stability parameters in the two-dimensional numerical model.

5.1. Model Validation and Stress Fluctuations

The frictional evolution of 75% quartz and 25% talc with a slip-weakening friction law and constant friction is used to validate the effect of the friction law. Figure 9 shows the comparison between friction evolution using both friction constitutive relations (slip weakening and constant) under a normal stress of 10 MPa. Both laws yield similar magnitudes of friction coefficient; however, the effect of instantaneous friction evolution is only

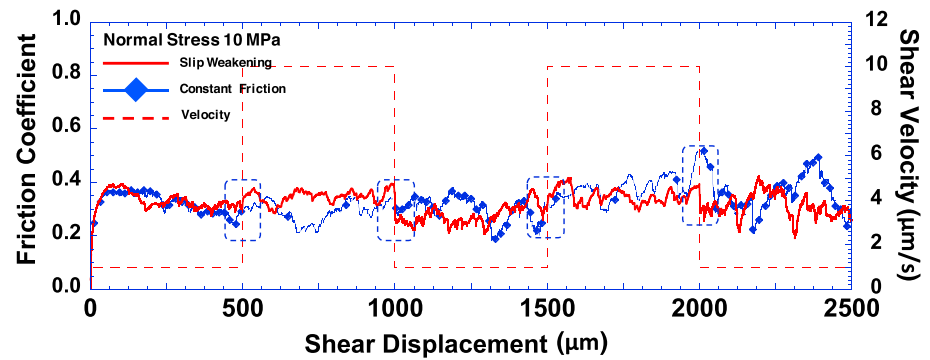


Figure 9. Contact model validation with comparison of velocity-stepping shear experiments on uniform mixtures with 75% quartz and 25% talc using models with a slip-weakening friction law or constant friction. The dashed rectangle highlights the frictional evolution after the velocity steps. Shear experiments with implemented slip-weakening model show clear frictional evolution at the velocity steps while it is difficult to observe a clear evolution of friction at velocity steps with a constant friction law.

observed while using a slip-weakening law. This identifies the key impact of the contact-contact slip-weakening law in defining ensemble behavior.

Both dimensionality and particle size have a major influence on fluctuations in friction evolution data [Knuth and Marone, 2007]. In 2-D laboratory experiments, it is common to observe frictional fluctuation magnitudes of 0.1–0.15. Our simulation results show similar or even smaller amplitudes of fluctuations.

Because the simulation results show relatively large fluctuations in the frictional evolution (of the order of 0.1–0.2), the resulting $(a - b)$ values need to be similarly scaled, which are 1 order of magnitude smaller than the fluctuations; they are originally too small and will be lost inside the noise should laboratory scale values be used (in the order of 0.001). Therefore, in order to capture the evolution of friction due to velocity changes, we implement $(a - b)$ values 1 magnitude larger than the laboratory measured $(a - b)$ values to capture the rate-and-state behavior. This is further discussed in section 5.7.

Large fluctuations are observed in frictional evolution in quartz-rich samples, especially in those with quartz content greater than 75%. This may be due to the nature of the 2-D configuration of this study. Particle dimensionality is associated with large fluctuations of shear strength especially in a 2-D configuration [Knuth and Marone, 2007]. However, the fluctuations in shear strength in talc-rich samples are much smaller than those in quartz-rich samples (this study). We believe there are two main governing factors influencing the shear strength fluctuations in our model, namely, particle abundance (particle sizing) and interparticle friction coefficient. Figures 10a and 10b show a comparison of frictional evolution of pure quartz during dynamic shearing with normal and reduced particle size (half of original particle size in this study; D_c value for quartz analog is adjusted accordingly). Smaller fluctuations are observed in the simulation with smaller particles. The magnitude of these fluctuations is not so significant in the context of this study compared to the exponentially increased computational cost in eliminating them. Interparticle friction coefficient is another important factor which may govern the fluctuations of the bulk shear strength. In this study, the mineral analogs are geometrically defined as circular particles without any angularity, with the rotation of particles also restricted. Therefore, interparticle friction coefficient may have a strong effect on the dilation behavior of particles. Figure 10b also shows frictional evolution of a quartz analog with artificially reduced interparticle friction coefficient (0.05), from which a reduction in shear strength fluctuation is observed. However, the ensemble shear strength is also reduced significantly with the reduction of interparticle friction coefficient.

5.2. Comparison With Established Rate and State Contact Models

Rate- and state-dependent frictional evolution has been previously implemented into particle dynamics simulations [Abe *et al.*, 2002]. A full rate and state constitutive relation was implemented at contact level in their approach, with the state variable θ (described in equation (5)) updated by local relative shear velocity and contact surface parameters. The contact model was implemented in a Lattice Solid Model, with

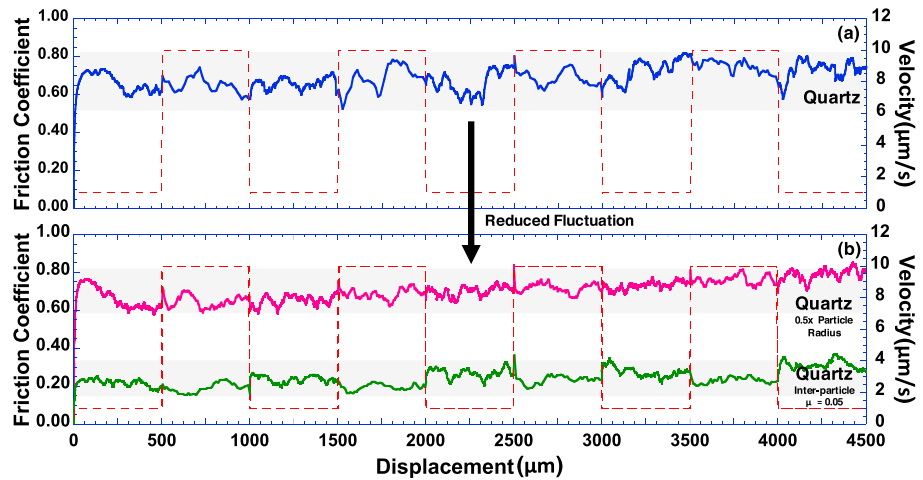


Figure 10. (a) Frictional evolution of pure quartz analog showing large fluctuations. (b) Frictional evolution of pure quartz analog with reduced particle size (0.5 times) and reduced interparticle friction coefficient (0.05) shows reduced fluctuations.

simulation results suggesting a good match with theoretical bare-surface rate and state models and laboratory experiments. The results also indicated that critical slip distance D_c is related to fault roughness. However, this approach is too computationally expensive to carry out using the large number of particles we use. Another approach [Morgan, 2004] simplified the complex rate and state constitutive relation by implementing a time-dependent frictional healing constitutive law onto contacts. The constitutive relation of friction in this model is described by equations (16) and (17) as follows:

$$\mu_p^a = \mu_p^0, t = 0 \tag{16}$$

$$\mu_p^a = \mu_p^0 + b \ln(t), t > 0 \tag{17}$$

where μ_p^a is the time-dependent interparticle friction coefficient and b is a scalar coefficient. This constitutive law was tested in a simulated gouge assembly consisting of circular-shaped particles with three different radii. Dynamic shear experiment under periodic boundary condition was conducted on the assembly to show that the model delivered a good match with laboratory hold-slide-hold experiments on fault gouge [Marone, 1998b].

The constitutive relation of friction described in this study is a slip-weakening law. Compared to the full implementation of rate and state friction law described above, the state variable θ is not included in the slip-weakening law due to the high computational cost to update θ on every contact through solving a series of nonlinear equations. Also, we do not implement time-dependent frictional healing onto each contact compared to the second example stated above. This will make the simulation of long-term friction evolution under hold-slide-hold conditions impractical for our model. However, the focus of this study is not in precisely simulating the micro-mechanisms of rate and state friction, implementing even second-order mechanisms. Instead, we simplify the problem by implementing a slip-weakening law to study instantaneous friction evolution response upon velocity steps and focus on the response of mineral mixtures. Our implementation is best suited for studying the transitional behavior of stability of minerals mixtures consisting of minerals with different stability parameters (a and b values). Additionally, our implementation also shows a good match with laboratory results of transitional behavior in stability using quartz and talc mixtures, which implies the validity and capacity of our simplification in predicting this transitional behavior of stability on mineral mixtures.

5.3. Shear Localization Within the Slip Zone and Effect of Shear Zone Thickness

In this study, numerical double direct shear tests are conducted on gouge mixtures with two representative structural distributions of talc. Observations suggest that the spatial distribution of talc has a strong influence

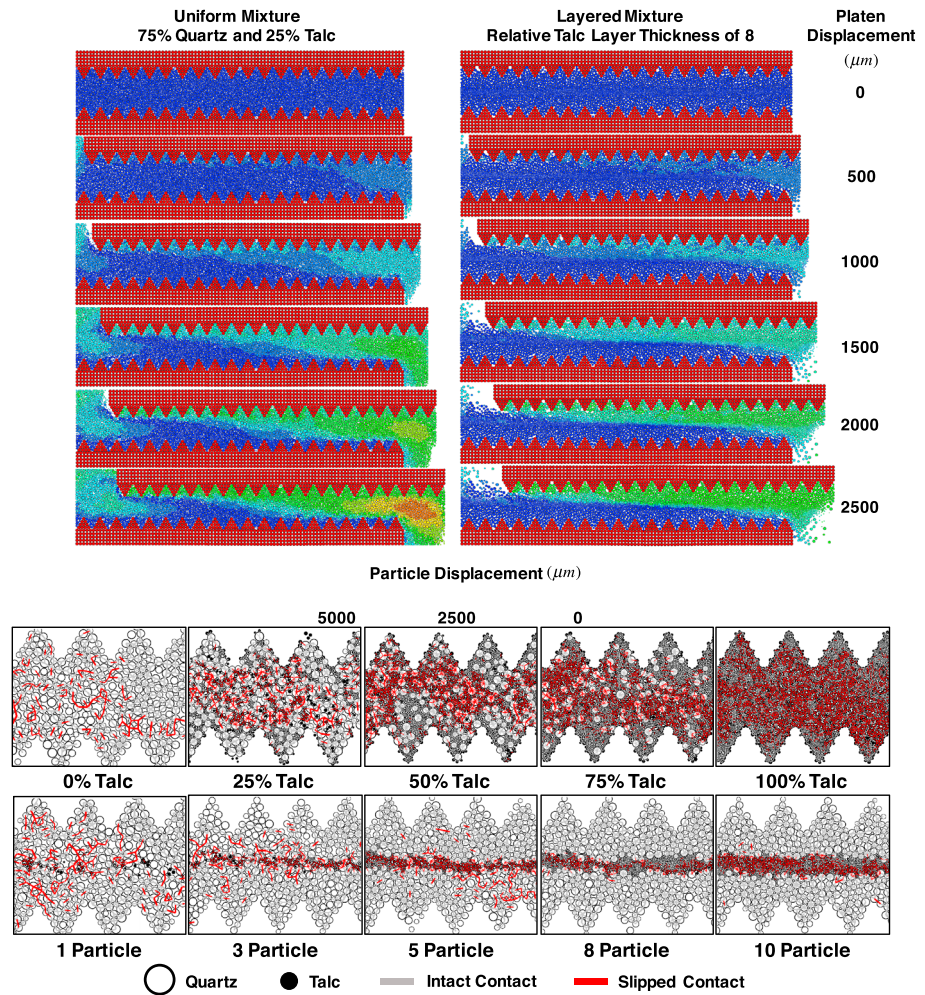


Figure 11. Displacement map of uniform mixture (75% quartz and 25% talc, Figure 11 (top left)) shows higher degree of particle rearrangement during shear, while layered mixture (relative layer thickness of 8, Figure 11 (top right)) shows distinctive shear localization along the intervening talc layer. Slipped contacts at the end stage (lower two rolls) of representative numerical runs. (top of lower two rolls) Representative plot of slipped contacts in uniform mixtures showing shear zones localized between the two shear platens. (bottom of lower two rolls) Representative plots of slipped contacts in layered mixtures showing shear zones localized inside or at the interfaces of the talc layer.

not only on the frictional strength but also on slip stability. These strong effects may be caused by enhanced shear localization corresponding to the spatial distribution of talc. Figure 11 shows a displacement map of the assembly (uniform mixture, 75% quartz and 25% talc; layered mixture, relative talc layer thickness of 8) and the distribution of slipped contacts at the end of representative numerical runs with both uniform (upper row) and textured mixtures (lower row). The displacement maps show that for uniform mixtures, there is a high degree of particle rearrangement, and shear planes are likely to form within the assembly (from upper left to lower right). However, for layered mixtures, the shear plane is more horizontal, matching the location of the talc layer. Therefore, we suggest that for uniform mixtures, the localization zones tend to bridge between the two shear platens with an inclined shear zone across the sample. For textured mixtures, the localization pattern appears to be similar to that for uniform mixtures with very little talc present in the sample (Figure 11, first column of the lower two rows). However, with a relative layer thickness larger than 3 particles, slip contacts are mainly present in the talc layer while few slipped contacts are present in the surrounding quartz matrix. This observation suggests that in structured (layered) samples, slip is easily mobilized on the interfaces or inside the weak layer. When slip events occur mostly on the layer interfaces or inside the weak layer, the bulk shear strength is governed by the weak layer and exhibits similar behavior to that for pure talc.

The same mechanism applies to the evolution of slip stability. Although talc exerts a strong influence on slip stability of the gouge, the scattered talc particles in uniform mixtures exert less impact on the bulk slip stability than the localized talc layer. This is mostly explained since slip tends to occur around and between talc particles due to the substantially lower contact friction. A thicker talc layer can greatly promote creep in the gouge, changing from velocity weakening to velocity strengthening. However, this transition is accompanied by a significant reduction in shear strength. Therefore, talc has a twofold influence: increasing the stability as evident in the ensemble parameters ($a - b$) but simultaneously reducing the shear strength of the fault.

These observed localization effects are consistent with those observed previously [Morgan, 2004]. In addition, previous studies also suggest that there is a localization effect on weakening as well, indicating that the slipped localization patch will become even weaker. In this study, we did not consider, at the contact level, the further weakening localization of a slipped weak patch since there is a further evolution law defined beyond slip weakening. This further effect in weakening is, however, out of the scope of our study. We consider the results and conclusions of this study, i.e., the transitional behavior of slip stability and evolution of transport behavior of mineral mixtures may not be heavily impacted by this further weakening of localization. This is due to the nature of this study which is focused on the bulk weakening effect of frictionally weak minerals.

Shear zone thickness is an important parameter to determine the relative shear velocity between particles. Thicker shear zones feature lower relative shear velocity between particles than thinner zones. In this study, the slip-weakening law is defined as global velocity and local strain based, i.e., the local friction evolution is calculated by the global reference velocity of the previous velocity step, the global load point velocity, local slip state, and local accumulated slip distance (described in section 2.1). We do not take into account local relative shear velocity. Therefore, shear zone thickness will not impose a significant effect on the results and conclusions of this study. This simplification is specific to this study, and shear zone thickness must be considered in the scenario of precisely modeling the rate and state behavior; however, this is beyond the scope of this study.

Grain shape is another important factor in controlling shear localization [Kock and Huhn, 2007]. Talc is a microscopically platy mineral, which is different from the circular-shaped particles we use in this study. However, despite the difference in representation, our simulation results of transitional behavior in shear strength and slip stability are consistent with previous laboratory experiments, which implies that circular-shaped particles may be sufficient in deriving the transitional behavior of mineral mixtures. Regardless, the effect of grain shape is important and needs to be further explored in DEM simulation.

5.4. Effect of System Stiffness and Platen Rigidity

In this work, a slip-weakening contact law is implemented rather than full rate-state behavior. Where we assume system stiffness to be infinitely large, this will always result in stable slip regardless of critical stiffness of the contact and sign of ($a - b$), although velocity-weakening behavior may still evolve; this will be an index of the potential for unstable behavior. Thus, this study contributes to the understanding of the true mechanism and potential for unstable behavior as there is an intrinsic system stiffness that must be accommodated in nature in assessing the potential for unstable slip. In other words, we use the metric of velocity/slip weakening as an absolute measure of the potential for unstable slip, unmodulated by an arbitrary system stiffness.

5.5. Dilation in Granular Systems Under Dynamic Shearing

As discussed in section 4, the initial strong dilation of quartz upon shearing is observed. This behavior is drastically different from the cyclic dilation compaction of talc in response to velocity up steps and velocity down steps. The mechanism of dilation/compaction and the concept of force chain generation and brittle failure has already been described in previous studies [Morgan and Boettcher, 1999; Anthony and Marone, 2005]. Essentially, in granular systems, dilation, compaction, and compliant shear deformation during dynamic shearing is governed by the generation and breakage of force chains. The same theory applies in our model. We propose that the differences in dilational behavior upon dynamic shearing may be due to differences in contact elastic stiffness and the interparticle friction coefficient. Quartz analog particles feature much higher contact stiffness (essentially effective modulus) and interparticle friction coefficient than talc analog particles

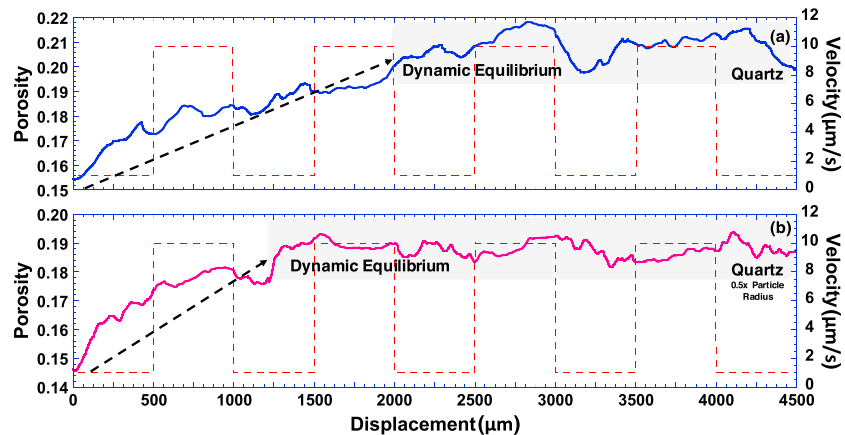


Figure 12. (a) Porosity evolution of pure quartz analog over a shear displacement of 4500 μm . Dynamic equilibrium is reached at ~ 2000 μm of shear displacement. (b) Porosity evolution of pure quartz analog with reduced particle radius over a shear displacement of 4500 μm , dynamic equilibrium is reached at ~ 1200 μm of shear displacement.

(refer to Table 1). High elastic stiffness and interparticle coefficients contribute to a higher degree of resistance in particle self-rearrangement during dynamic shearing, thus promoting strong dilation. Furthermore, this high resistance in self-rearrangement may delay the prompt reaction to changes in shear velocity. This may be the reason that no significant compaction is observed during velocity down steps in the quartz-rich samples. This may also explain the large initial dilation of pure quartz and the quartz-rich analog during dynamic shearing since it takes more shear displacement for the particles in these assemblies to reach a dynamic equilibrium. In contrast, talc particles feature a significantly lower contact stiffness and interparticle friction coefficient, which greatly reduces the resistance to particle self-rearrangement during dynamic shearing. Therefore, the assembly reacts more quickly to changes in shear velocity. The self-rearrangement resistance can also be affected by the abundance of particles. Figure 12a shows the evolution of porosity of pure quartz over 4500 μm of shear displacement. The porosity evolution of quartz with reduced particle size is also shown Figure 12b. It can be clearly observed that for a quartz assembly, with half-sized particles (more particles overall), after ~ 1200 μm of shear displacement the assembly reaches a dynamic equilibrium as indicated by a halted increase in overall porosity. This is significantly faster than the original evolution of pure quartz (~ 2000 μm) in reaching dynamic equilibrium. But in both cases, the tendency of dilation in quartz is strong and the porosity evolution is of similar magnitude.

In the quartz-talc analog mixtures, the interparticle elastic stiffness of a quartz-talc contact is taken by connecting the contact stiffness of quartz and talc in series, with the interparticle friction coefficient taken as the minimum of the two. In this case, talc will dominate in determining the contact stiffness. Essentially, this will cause increased weakening on the quartz particles connected by talc particles (due to lowered contact elastic stiffness and talc-dependent interparticle friction coefficient). Meanwhile, the reduction in interparticle friction coefficient and elastic stiffness also contributes to the reduction in resistance to self-rearrangement during dynamic shearing, thereby reducing the dilation tendency, which eventually leads to the transition from strong dilation (pure quartz) to cyclic dilation and compaction (pure talc).

There are other properties affecting the dilation of granular assemblies, such as particle shape, angularity, and surface roughness. The study of the effects of these multiple parameters is important to illuminate mechanisms of the shearing of granular materials, but it is beyond the scope of this study.

5.6. Stability of Slip Events

Slip events at contacts may and will occur in the gouge assembly once shear begins. It is worth noting that not all contacts will slip at once under dynamic shearing due to particle packing and local effects. Slip is triggered once the Coulomb criterion is reached locally and evolves according to a prescribed slip-weakening law as the slip proceeds. Once local slip occurs, under the assumption that the system stiffness is infinite, the calculated slip at the sliding contact will always be stable but will evolve to a new state following the

slip-weakening law and according to local slip distance. However, if local contact slip does not occur at a given time, the friction coefficient will remain constant and not evolve. In any fault gouge sample, there are both contacts undergoing slip as well as those that are stationary. Therefore, the ensemble friction evolution is a combination of local friction evolution (either undergoing slip weakening or not) of every contact in the assembly.

5.7. Scaling of Empirical Stability Parameters and Uncertainties

In the DEM model, there are inevitable differences and conversions between grain-grain scale mechanical parameters and macroscopic mechanical parameters. For example, the macroscopic elastic modulus is converted into an effective modulus, and through normal-to-shear stiffness ratio, effective modulus is then converted to normal and shear contact stiffness. These conversions map the grain-grain scale parameters from macroscopic parameters. The same rules also apply to stability parameters. Considering the fluctuation of the 2-D numerical shear model, the stability parameters measured from the bulk stability evolution data differ from those used at grain-grain scale. Particularly, the stability parameters from curve fitting are of similar magnitude (0.01–0.05) to the stability parameters assigned at grain-grain scale. They are, however, 1 order of magnitude larger than the laboratory measured parameters shown in Figure 5b (0.001–0.008). This is due to the two-dimensional configuration generating a relatively large amount of noise in the frictional evolution [Knuth and Marone, 2007], which prevents clear analysis of stability parameters at the laboratory scale. Therefore, the use of relatively large and artificial stability parameters in two-dimensional models helps to identify the transitional behaviors in frictional strength and slip stability.

Uncertainties remain since simplifications and assumptions have been made for this numerical study. Specifically, the mineral particles are assumed to be circular and a slip-weakening constitutive relation has been taken as a simplification of rate and state constitutive behavior. These assumptions, might not be applicable in every situation but serve well in reproducing the transitional behavior of shear strength and slip stability of frictionally strong/weak mineral mixtures, as well as predicting evolutionary trends in permeability. Besides, the method we use to calculate the resultant stability parameters for quartz-talc mineral contacts reveals a potential relation of the resultant stability parameters of contacts between surfaces with drastically different stability properties.

6. Conclusions

A DEM model is established to simulate the mechanical responses of synthetic gouge mixtures consisting of quartz and talc analogs. Direct shear experiments with predefined velocity up steps and down steps were conducted on both uniform and textured mixtures. This is achieved by altering the weight percentage of talc in uniform mixtures and the relative thickness of the talc layer in textured (layered) mixtures and in then analyzing experimental results. The following conclusions are drawn:

1. Talc has a significant weakening effect on the shear strength of quartz-rich fault gouges. This effect is enhanced when talc forms a through-going layer in the gouge.
2. Relatively small amounts of talc (10% to 25% talc in the uniform mixtures or 3 particles to 5 particles in the textured mixtures) can transform the stability behavior of the gouge from velocity weakening to velocity strengthening.
3. Minerals with high elastic modulus and frictional resistance at contacts tend to dilate universally upon slip, while minerals with low elastic modulus and frictional resistance dilate during velocity up steps but compact quickly during velocity down steps.
4. Quartz tends to be dilation dominant, and thus, an increase in permeability could be expected in quartz-rich faults during slip events; while talc also dilates, but compacts much faster, therefore, a decrease in permeability could be expected in talc-bearing faults.

The numerical modeling-derived conclusions suggest that DEM modeling is capable of simulating the shear strength and stability evolution of granular fault gouge using a simplified rate-state friction law. Also, it is possible to simulate gouge with complex mineralogical composition and with varying degrees and forms of heterogeneity. The analysis of coordination number and porosity evolution suggests new methods to examine the nature of permeability evolution of faults during the seismic cycle.

Acknowledgments

This work is the result of support provided by DOE Grant DE-FE0023354. This support is gratefully acknowledged. This work utilizes data from literature which are cited in the main reference list; data from numerical modeling of this study are shown in the main text.

References

- Abe, S., and K. Mair (2009), Effects of gouge fragment shape on fault friction: New 3D modelling results, *Geophys. Res. Lett.*, *36*, L23302, doi:10.1029/2009GL040684.
- Abe, S., J. H. Dieterich, P. Mora, and D. Place (2002), Simulation of the influence of rate- and state-dependent friction on the macroscopic behavior of complex fault zones with the lattice solid model, *Pure Appl. Geophys.*, *159*(9), 1967–1983, doi:10.1007/s00024-002-8718-7.
- Abe, S., H. van Gent, and J. L. Urai (2011), DEM simulation of normal faults in cohesive materials, *Tectonophysics*, *512*(1–4), 12–21, doi:10.1016/j.tecto.2011.09.008.
- Ampuero, J. P., and Y. Ben-zion (2008), Cracks, pulses and macroscopic asymmetry of dynamic rupture on a bimaterial interface with velocity-weakening friction, *Geophys. J. Int.*, *173*(2), 674–692, doi:10.1111/j.1365-246X.2008.03736.x.
- Anthony, J. L., and C. Marone (2005), Influence of particle characteristics on granular friction, *J. Geophys. Res.*, *110*, B08409, doi:10.1029/2004JB003399.
- Antonellini, M. A., and D. D. Pollard (1995), Distinct element modeling of deformation bands in sandstone, *J. Struct. Geol.*, *17*(8), 1165–1182, doi:10.1016/0191-8141(95)00001-T.
- Bos, B., and C. J. Spiers (2002), Frictional-viscous flow of phyllosilicate-bearing fault rock: Microphysical model and implications for crustal strength profiles, *J. Geophys. Res.*, *107*(B2), 2028, doi:10.1029/2001JB000301.
- Burbidge, D. R., and J. Braun (2002), Numerical models of the evolution of accretionary wedges and fold-and-thrust belts using the distinct-element method, *Geophys. J. Int.*, *148*(3), 542–561, doi:10.1046/j.1365-246x.2002.01579.x.
- Carpenter, B. M., C. Marone, and D. M. Saffer (2009), Frictional behavior of materials in the 3D SAFOD volume, *Geophys. Res. Lett.*, *36*, L05302, doi:10.1029/2008GL036660.
- Collettini, C., A. Niemeijer, C. Viti, and C. Marone (2009), Fault zone fabric and fault weakness, *Nature*, *462*(7275), 907–910, doi:10.1038/nature08585.
- Cundall, P. A., and O. D. L. Strack (1979), A discrete numerical model for granular assemblies, *Géotechnique*, *29*(1), 47–65, doi:10.1680/geot.1979.29.1.47.
- Dieterich, J. H. (1978), Time-dependent friction and the mechanics of stick-slip, *Pure Appl. Geophys. PAGEOPH*, *116*(4–5), 790–806, doi:10.1007/BF00876539.
- Dieterich, J. H. (1979a), Modeling of rock friction 1. Experimental results and constitutive equations, *J. Geophys. Res.*, *84*(B5), 2161–2168, doi:10.1029/JB084iB05p02161.
- Dieterich, J. H. (1979b), Modeling of rock friction 2. Simulation of preseismic slip, *J. Geophys. Res.*, *84*(B5), 2169–2175, doi:10.1029/JB084iB05p02169.
- Di Toro, G., T. Hirose, S. Nielsen, G. Pennacchioni, and T. Shimamoto (2006), Natural and experimental evidence of melt lubrication of faults during earthquakes, *Science*, *311*(5761), 647–649, doi:10.1126/science.1121012.
- Engelder, J. T., J. M. Logan, and J. Handin (1975), The sliding characteristics of sandstone on quartz fault-gouge, *Pure Appl. Geophys. PAGEOPH*, *113*(1), 69–86, doi:10.1007/BF01592900.
- Fang, Y., D. Elsworth, C. Wang, T. Ishibashi, and J. P. Fitts (2017), Frictional stability-permeability relationships for fractures in shales, *J. Geophys. Res. Solid Earth*, *122*, 1760–1776, doi:10.1002/2016JB013435.
- Faulkner, D. R., and E. H. Rutter (2001), Can the maintenance of overpressured fluids in large strike-slip fault zones explain their apparent weakness?, *Geology*, *29*(6), 503–506, doi:10.1130/0091-7613(2001)029<0503:CTMOOF>2.0.CO;2.
- Guan, C., J. Qi, N. Qiu, G. Zhao, Q. Yang, X. Bai, and C. Wang (2012), Macroscopic Young's elastic modulus model of particle packing rock layers, *Open J. Geol.*, *2*(July), 198–202, doi:10.4236/ojg.2012.23020.
- Guo, Y., and J. K. Morgan (2004), Influence of normal stress and grain shape on granular friction: Results of discrete element simulations, *J. Geophys. Res.*, *109*, B12305, doi:10.1029/2004JB003044.
- Hieher, P. Y. (1996), Elastic properties of soils, *J. Geotech. Eng.*, *122*(August), 641–648.
- Ikari, M. J., C. Marone, and D. M. Saffer (2011), On the relation between fault strength and frictional stability, *Geology*, *39*(1), 83–86, doi:10.1130/G31416.1.
- Knuth, M., and C. Marone (2007), Friction of sheared granular layers: Role of particle dimensionality, surface roughness, and material properties, *Geochem. Geophys. Geosyst.*, *8*, Q03012, doi:10.1029/2006GC001327.
- Kock, I., and K. Huhn (2007), Numerical investigation of localization and micromechanics in a stratified soil specimen, *J. Struct. Geol.*, *29*(10), 1679–1694, doi:10.1016/j.jsg.2007.07.013.
- Mair, K., and C. Marone (1999), Friction of simulated fault gouge for a wide range of velocities and normal stresses, *J. Geophys. Res.*, *104*(B12), 28,899–28,914, doi:10.1029/1999JB900279.
- Marone, C. (1998a), Laboratory-derived friction laws and their application to seismic faulting, *Annu. Rev. Earth Planet. Sci.*, *26*(1), 643–696, doi:10.1146/annurev.earth.26.1.643.
- Marone, C. (1998b), The effect of loading rate on static friction and the rate of fault healing during the earthquake cycle, *Nature*, *391*(6), 69–72, doi:10.1038/nature34157.
- Marone, C., C. B. Raleigh, and C. H. Scholz (1990), Frictional behavior and constitutive modeling of simulated fault gouge, *J. Geophys. Res.*, *95*(B5), 7007–7025, doi:10.1029/JB095iB05p07007.
- Melosh, H. J. (1996), Dynamic weakening of faults by acoustic fluidization, *Nature*, *379*(February 1996), 601, doi:10.1038/379601a0.
- Moore, D. E., and D. A. Lockner (2011), Frictional strengths of talc-serpentine and talc-quartz mixtures, *J. Geophys. Res.*, *116*, B01403, doi:10.1029/2010JB007881.
- Moore, D. E., and M. J. Rymer (2007), Talc-bearing serpentine and the creeping section of the San Andreas Fault, *Nature*, *448*(7155), 795–797, doi:10.1038/nature06064.
- Morgan, J. K. (1999), Numerical simulations of granular shear zones using the distinct element method 2. Effects of particle size distribution and interparticle, *J. Geophys. Res.*, *104*(B2), 2721–2732.
- Morgan, J. K. (2004), Particle dynamics simulations of rate- and state-dependent frictional sliding of granular fault gouge, *Pure Appl. Geophys.*, *161*(9–10), 1877–1891, doi:10.1007/s00024-004-2537-y.
- Morgan, J. K., and M. S. Boettcher (1999), Numerical simulations of granular shear zones using the distinct element method: 1. Shear zone kinematics and the micromechanics of localization, *J. Geophys. Res.*, *104*(B2), 2703–2719, doi:10.1029/1998JB900056.
- Morgan, J. K., and P. J. McGovern (2005), Discrete element simulations of gravitational volcanic deformation: 1. Deformation structures and geometries, *J. Geophys. Res.*, *110*, B05402, doi:10.1029/2004JB003252.
- Niemeijer, A., C. Marone, and D. Elsworth (2010), Fabric induced weakness of tectonic faults, *Geophys. Res. Lett.*, *37*, L03304, doi:10.1029/2009GL041689.

- Niemeijer, A. R., and C. J. Spiers (2006), Velocity dependence of strength and healing behaviour in simulated phyllosilicate-bearing fault gouge, *Tectonophysics*, 427(1–4), 231–253, doi:10.1016/j.tecto.2006.03.048.
- Ouyang, Z., and D. Elsworth (1993), Evaluation of groundwater flow into mined panels, *Int. J. Rock Mech. Min. Sci.*, 30(2), 71–79, doi:10.1016/0148-9062(93)90701-E.
- Press, W., S. Teukolsky, W. Vetterling, B. Flannery, E. Ziegel, W. Press, B. Flannery, S. Teukolsky, and W. Vetterling (1987), Numerical recipes: The art of scientific computing.
- Rathbun, A. P., F. Renard, and S. Abe (2013), Numerical investigation of the interplay between wall geometry and friction in granular fault gouge, *J. Geophys. Res. Solid Earth*, 118, 878–896, doi:10.1002/jgrb.50106.
- Rice, J. R. (1992), Fault stress states, pore pressure distributions, and the weakness of the San Andreas Fault.
- Ruina, A. (1983), Slip instability and state variable friction law, *J. Geophys. Res.*, 88, 10,359–10,370, doi:10.1029/JB088iB12p10359.
- Samuelson, J., D. Elsworth, and C. Marone (2011), Influence of dilatancy on the frictional constitutive behavior of a saturated fault zone under a variety of drainage conditions, *J. Geophys. Res.*, 116, B10406, doi:10.1029/2011JB008556.
- Scholz, C. H. (1998), Earthquakes and friction laws, *Nature*, 391(6662), 37–42, doi:10.1038/34097.
- Sun, Z., D. N. Espinoza, and M. T. Balhoff (2016), Discrete element modeling of indentation tests to investigate mechanisms of CO₂-related chemomechanical rock alteration, *J. Geophys. Res. Solid Earth*, 121, 7867–7881, doi:10.1002/2016JB013554.

Erratum

In the originally published version of this article, Equation (16) contained a subtraction sign that should be an equal sign. The equation has been corrected, and this version may be considered the authoritative version of record.